8
Computational Fluid Dynamics of Catalytic Reactors

Vinod M. Janardhanan and Olaf Deutschmann

8.1
Introduction

Catalytic reactors are generally characterized by the complex interaction of various physical and chemical processes. Monolithic reactors can serve as example, in which partial oxidation and reforming of hydrocarbons, combustion of natural gas, and reduction of pollutant emissions from automobiles are frequently carried out. Figure 8.1 illustrates the physics and chemistry in a catalytic combustion monolith that glows at a temperature of about 1300 K due to the exothermic oxidation reactions. In each channel of the monolith, the transport of momentum, energy, and chemical species occurs not only in flow (axial) direction but also in radial direction. The reactants diffuse to the inner channel wall, which is coated with the catalytic material, where the gaseous species adsorb and react on the surface. The products and intermediates desorb and diffuse back into the bulk flow. Due to the high temperatures, the chemical species may also react homogeneously in the gas phase. In catalytic reactors, the catalyst material is often dispersed in porous structures such as washcoats or pellets. Mass transport in the fluid phase and chemical reactions are then superimposed by diffusion of the species to the active catalytic centers in the pores. The temperature distribution depends on the interaction of heat convection and conduction in the fluid, heat release due to chemical reactions, heat transport in the solid material, and thermal radiation. If the feed conditions vary in time and space and/or heat transfer occurs between the reactor and the ambience, a nonuniform temperature distribution over the entire monolith will result, and the behavior will differ from channel to channel.

Today, the challenge in catalysis is not only the development of new catalysts to synthesize a desired product but also the understanding of the interaction of the catalyst with the surrounding reactive flow field. Sometimes, the exploitation of these interactions can lead to the desired product selectivity and yield. Hence, a better understanding of gas–solid flows in chemical reactors is understood as a critical need in chemical technology calling for the development of reliable simulation tools that

Modeling and Simulation of Heterogeneous Catalytic Reactions: From the Molecular Process to the Technical System, First Edition. Edited by Olaf Deutschmann.

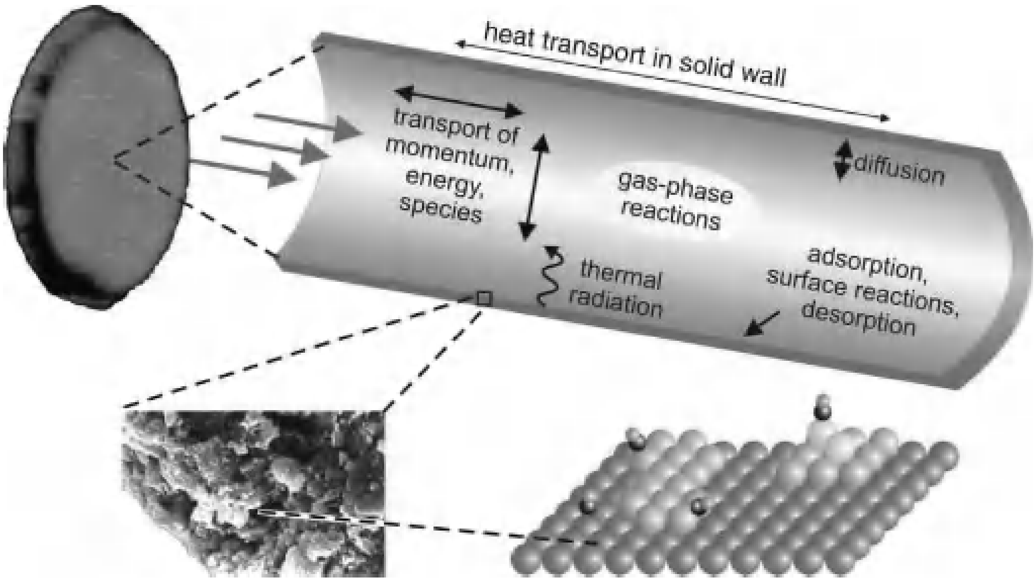

Figure 8.1 Catalytic combustion monolith and physical and chemical processes occurring in the single monolith channel.

integrate detailed models of reaction chemistry and computational fluid dynamics (CFD) modeling of macroscale flow structures.

Computational fluid dynamics is able to predict very complex flow fields, even combined with heat transport, due to the recently developed numerical algorithms and the availability of faster and bigger (memory) computer hardware. The consideration of detailed models for chemical reactions, in particular for heterogeneous reactions, however, is still very challenging due to the large number of species mass conservation equations, their highly nonlinear coupling, and the wide range of timescales introduced by the complex reaction networks.

This chapter introduces the application of CFD simulations to obtain a better understanding of the interactions between mass and heat transport and chemical reactions in catalytic reactors. Concepts for modeling and numerical simulation of catalytic reactors are presented, which describe the coupling of the physical and chemical processes in detail. The elementary kinetics and dynamics as well as ways for modeling the intrinsic chemical reaction rates (microkinetics) by various approaches such as Monte Carlo (MC), mean field approximation (MF), and lumped kinetics are discussed in the earlier chapters of this book. In this chapter, it is assumed that models exist that can compute not only the local heterogeneous but also the homogeneous reaction rate as function of the local conditions such as temperature and species concentrations in the gas phase and of the local and temporal state of the catalyst. These chemical source terms are here coupled with the fluid flow and used to numerically simulate the catalytic reactor.

The ultimate objective of CFD simulations of catalytic reactors is (1) to understand the interactions of physics (mass and heat transport) and chemistry in the reactor, (2) to support reactor design and engineering, and (3) eventually, to find optimized operating conditions for maximization of the desired product's yield and minimization of undesired side products and/or pollutants. Though computational fluid dynamics covers a wide range of problems, ranging from simulation of the flow around airplanes to laminarization of turbulent flows entering a microchannel, this chapter focuses on the principal ideas and the potential applications of CFD in heterogeneous catalysis; textbooks [1, 2] and specific literature are frequently referenced for more details. Specific examples taken from literature and our own work will be used for illustration of the state-of-the-art CFD simulation of chemical reactors with heterogeneously catalyzed reactions. The next chapters of the book will cover some specific topics of numerical simulation of catalytic reactors in more detail.

8.2 Modeling of Reactive Flows

8.2.1 Governing Equations of Multicomponent Flows

As long as a fluid can be treated as a continuum, the most accurate description of the flow field of multicomponent mixtures is given by the transient three-dimensional (3D) Navier–Stokes equations coupled with the energy and species governing equations, which will be summarized in this section. More detailed introduction to fluid dynamics and transport phenomena can be found in a number of textbooks [1–5]. Other alternative concepts such as Lattice-Boltzmann models have also been discussed for simulation of catalytic reactors as introduced in Section 8.4.1.

Governing equations, which are based on conservation principles, can be derived by consideration of the flow within a certain spatial region, which is called the *control volume*.

The principle of mass conservation leads to the mass continuity equation

$$\frac{\partial \varrho}{\partial t} + \frac{\partial(\varrho v_i)}{\partial x_i} = S_{\mathrm{m}}, \tag{8.1}$$

with ϱ being the mass density, t the time, x_i ($i = 1,2,3$) are the Cartesian coordinates, and v_i the velocity components. The source term S_{m} vanishes unless mass is either deposited on or ablated from the solid surfaces. The Einstein convention is used here, that is, whenever the same index appears twice in any term, summation over that index is implied, except when the index refers to a chemical species. The principle of momentum conservation for Newtonian fluids leads to three scalar equations for the momentum components ϱv_i

$$\frac{\partial(\varrho v_i)}{\partial t} + \frac{\partial(\varrho v_i v_j)}{\partial x_j} + \frac{\partial p}{\partial x_i} + \frac{\partial \tau_{ij}}{\partial x_j} = \varrho g_i, \tag{8.2}$$

where p is the static pressure, τ_{ij} is the stress tensor, and g_i are the components of the gravitational acceleration. The above equation is written for Cartesian coordinates. Gravity, the only body force taken into account, can often be neglected when modeling catalytic reactors. The stress tensor is given as

$$\tau_{ij} = -\mu\left(\frac{\partial v_i}{\partial x_j} + \frac{\partial v_j}{\partial x_i}\right) + \left(\frac{2}{3}\mu - \kappa\right)\delta_{ij}\frac{\partial v_k}{\partial x_k}. \tag{8.3}$$

Here, κ and μ are the bulk viscosity and mixture viscosity, respectively, and δ_{ij} is the Kronecker delta, which is unity for $i = j$, else zero. The bulk viscosity vanishes for low-density monoatomic gases and is also commonly neglected for dense gases and liquids [1]. The coupled mass continuity and momentum governing equations have to be solved for the description of the flow field.

In multicomponent mixtures, not only the flow field is of interest but also the mixing of the chemical species and reactions among them, which can be described by an additional set of partial differential equations. Here, the mass m_i of each of the N_g gas-phase species obeys a conservation law that leads to

$$\frac{\partial(\varrho Y_i)}{\partial t} + \frac{\partial(\varrho v_j Y_i)}{\partial x_j} + \frac{\partial(j_{i,j})}{\partial x_j} = R_i^{\text{hom}}, \tag{8.4}$$

with Y_i is the mass fraction of species i in the mixture ($Y_i = m_i/m$) with m as total mass, R_i^{hom} is the net rate of production due to homogeneous chemical reactions. The components $j_{i,j}$ of the diffusion mass flux caused by concentration and temperature gradients are often modeled by the mixture average formulation [6]:

$$j_{i,j} = -\varrho\frac{Y_i}{X_i}D_i^{\text{M}}\frac{\partial X_i}{\partial x_j} - \frac{D_i^{\text{T}}}{T}\frac{\partial T}{\partial x_j}. \tag{8.5}$$

D_i^{M} is the effective diffusion coefficient of species i in the mixture, D_i^{T} is the thermal diffusion coefficient, which is significant only for light species, and T is the temperature. The molar fraction X_i is related to the mass fraction Y_i using the species molar masses M_i by

$$X_i = \frac{1}{\sum_{j=1}^{Ng} Y_j/M_j}\frac{Y_i}{M_i}. \tag{8.6}$$

Heat transport and heat release due to chemical reactions lead to spatial and temporal temperature distributions in catalytic reactors. The corresponding governing equation for energy conservation is commonly expressed in terms of the specific enthalpy h:

$$\frac{\partial(\varrho h)}{\partial t} + \frac{\partial(\varrho v_j h)}{\partial x_j} + \frac{\partial j_{q,j}}{\partial x_j} = \frac{\partial p}{\partial t} + v_j\frac{\partial p}{\partial x_j} - \tau_{jk}\frac{\partial v_j}{\partial x_k} + S_{\text{h}}, \tag{8.7}$$

with S_{h} being the heat source, for instance, due to thermal radiation. In multicomponent mixtures, diffusive heat transport is significant due to heat conduction and mass diffusion, hence

$$j_{q,j} = -\lambda\frac{\partial T}{\partial x_j} + \sum_{i=1}^{Ng} h_i j_{i,j}. \tag{8.8}$$

Here, λ is the thermal conductivity of the mixture. The temperature is then related to the enthalpy by the definition of the mixture-specific enthalpy

$$h = \sum_{i=1}^{Ng} Y_i h_i(T), \tag{8.9}$$

with h_i being the specific enthalpy of species i, which is a monotonic increasing function of temperature. The temperature is then commonly calculated from Eq. (8.9) for known h and Y_i by employing a root finding algorithm.

Heat transport in solids such as reactor walls and catalyst materials can also be modeled by an enthalpy equation, for instance, in the form of

$$\frac{\partial(\varrho h)}{\partial t} - \frac{\partial}{\partial x_j}\left(\lambda \frac{\partial T}{\partial x_j}\right) = S_\mathrm{h}, \tag{8.10}$$

where h is the specific enthalpy and λ the thermal conductivity of the solid material. S_h accounts for heat sources, for instance, due to heat release by chemical reactions and electric or radiative heating of the solid.

This system of governing equations is closed by the equation of state to relate the thermodynamic variable density ϱ, pressure p, and temperature T. The simplest model of this relation for gaseous flows is the ideal gas equation

$$p = \frac{\varrho R T}{\sum_{i=1}^{N_\mathrm{g}} X_i M_i}, \tag{8.11}$$

with the universal gas constant $R = 8.314\,\mathrm{J/(mol\,K)}$.

The transport coefficients μ, D_i^M, D_i^T, and λ appearing in Eqs. (8.3), (8.5), and (8.8) depend on temperature and mixture composition. They are derived from the transport coefficients of the individual species and the mixture composition by applying empirical approximations [1, 2, 4], which eventually lead to two physical parameters for each species, a characteristic diameter (the Lennard–Jones collision diameter), σ_i, and a characteristic energy (the Lennard–Jones potential well depth), ε_i, which can be taken from databases [7].

The specific enthalpy h_i is a function of temperature and can be expressed in terms of the heat capacity

$$h_i = h_i(T_\mathrm{ref}) + \int_{T_\mathrm{ref}}^{T} c_{p,i}(T')\mathrm{d}T', \tag{8.12}$$

where $c_{p,i}$ is the specific heat capacity at constant pressure. The specific standard enthalpy of formation $\Delta h^0_{\mathrm{f},298,i}$ can be used as integration constant $h_i(T_\mathrm{ref} = 298.15\,\mathrm{K}$, $p_0 = 1\,\mathrm{bar})$. Experimentally determined and estimated standard enthalpies of formation, standard entropies, and temperature-dependent heat capacities can be found in databases [8–10] or estimated by Benson's additivity rules [11].

8.2.2
Turbulent Flows

Turbulent flows are characterized by continuous fluctuations of velocity, which can lead to fluctuations in scalars such as density, temperature, and mixture composition. Turbulence can be desired in catalytic reactors to enhance mixing and reduce mass transfer limitations, but can be unwanted due to the increased pressure drop and energy dissipation. An adequate understanding of all facets of turbulent flows is still lacking [4, 12, 13]. In the area of catalytic systems, some progress has recently been made in turbulent flow modeling, for example, in catalytically stabilized combustion [14, 15]. The Navier–Stokes equations as presented above are, in principle, able to model turbulent flows (direct numerical simulation). However, in practice, the solutions of the Navier–Stokes equations for turbulent flows in technical reactors demand a prohibitive amount of computational time due to the huge number of grid points needed to resolve the small scales of turbulence. Therefore, several concepts were developed to model turbulent flows by the solution of averaged governing equations. However, the equation system is not closed, meaning that a model has to be set up to describe the so-called Reynold stresses that are the correlations between the velocity fluctuations and the fluctuations of all the quantities of the flow (velocity, enthalpy, and mass fractions). The $k - \varepsilon$ model [16] is one of the most widely used concept for modeling the Reynold stresses at high Reynolds numbers, which adds two additional partial differential equations for the description of the turbulent kinetic energy, k, and the dissipation rate, ε, to the governing equations. Although the model has well-known deficiencies, it is today implemented in most commercial CFD codes and also widely used for the simulation of catalytic reactors. Recently, turbulent flow field simulations are often based on large-eddy simulation (LES), which combines DNS for the larger scales with a turbulence model, for example, $k - \varepsilon$ model, for the unresolved smaller scales.

Aside form this closure problem, one still has to specify the averaged chemical reaction rates [4, 12]. Because of the strong nonlinearity of the rate coefficients due to the exponential dependence on temperature and the power law dependence on partial pressure, the source terms of chemical reactions in turbulent flows cannot be computed using average concentrations and temperature. Here, probability density functions (PDFs) [4], either derived by transport equations [13] or empirically constructed [17], are used to take the turbulent fluctuations into account when calculating the chemical source terms. For the simulation of reactions on catalysts, it is important to use appropriate models for the flow laminarization at the solid surface.

8.2.3
Three-Phase Flow

Three-phase flows involve the participation of solid, liquid, and gaseous phases. In certain cases, the solid phase will be a porous medium, and the fluids will flow though the pore networks. In certain other cases, all phases will be mobile and these flows are usually characterized by various regimes such as particle-laden flow, fluidized bed flow, slug flow, bubbly flow, and so on. Examples for three-phase flow devices with chemical reactions are fluidized bed reactors. They are one of the most important classes of multiphase reactors used in chemical, petrochemical, and biochemical processing. Simulating multiphase reactors is a challenge due to the numerous physicochemical processes occurring in the reactor. For example, one has to account for interactions between and among various phases, lift, buoyancy, virtual mass forces, particle agglomeration, and bubble coalescence [18].

Either the Euler–Lagrange model or Euler–Euler model can be used to solve the three-phase flow problem. The former adopts a continuum description for the liquid phase and tracks the discrete phases using Lagrangian particle trajectory analysis. The Euler–Euler model is based on the concept of interpenetrating continua. Here, all the phases are treated as continua with properties analogous to those of a fluid. That is, conservation equations are derived for each of the phases and constitutive relations that are empirical in nature closes the equation set. Therefore, the accuracy of this method heavily relies on the empirical constitutive relations used. Furthermore, this approach has limitation in predicting certain characteristics of discrete flow. For instance, the method cannot account for particle size effects, particle agglomeration, bubble coalescence, and bubble breakage. On the other hand, the Euler–Lagrange model has empirical equations and can provide detailed information of discrete phases. However, it is computationally more expensive. A detailed description of three-phase flow modeling is beyond the scope of this chapter and interested readers can refer to textbooks [19–21].

8.2.4
Momentum and Energy Equations for Porous Media

Porous media are present everywhere in catalytic reactors [22, 23], for instance, fixed bed reactors, catalytic filters, washcoat layers, perforated plates, flow distributors, tube banks, membranes, electrodes, fiber materials, and so on. Modeling the transport and reactions in the actual tortuous structure on the microscopic level is a rather formidable task [23, 24]. Chapter 5 of this book deals in detail with this topic. Due to this complexity, it is often necessary to work with small representative volume elements where the porous medium and other properties are assumed to be homogenized. Several methods have been developed to include porous media and reactions in CFD simulations.

Most porous media models in CFD codes incorporate an empirically determined flow resistance accounting for the pressure drop, which is a sink in the governing momentum equation (8.2). In case of simple homogeneous porous media, a source term is added to the right side of Eq. (8.2),

$$S_i = -\left(\frac{\mu}{\alpha} v_i + \frac{C}{2} \varrho |\vec{v}| v_i\right), \tag{8.13}$$

where α is the permeability (Darcy's law) and C is the inertial resistance, which can be viewed as a loss per unit length along the flow direction. Concerning the temperature profile in porous media, the enthalpy equations (8.7) and (8.10) have to be adapted.

The total enthalpy is now a sum of the enthalpies of the fluid and the solid. Their partition is defined by porosity. An effective thermal conductivity is used based on the porosity and the thermal conductivities of the fluid and the solid. This continuum approach has to be used carefully; for instance, the effect of the porous medium on turbulent flows can be barely approximated within this concept. The approach, which assumes constant unidirectional flow, also breaks down for fixed bed reactors with reactor diameter being less than ten times the particle size. Thus, the model cannot predict the velocity maximum in the vicinity of the wall observed experimentally for those reactors [25]. An averaged velocity with a radial varying axial component can be provided by further modification of the momentum balance [25–27] as improvement of the classical model.

8.3 Coupling of the Flow Field with Heterogeneous Chemical Reactions

Depending on the spatial resolution of the different catalyst structures such as flat surface, gauzes, single pellets, and in porous media, the species mass fluxes due to catalytic reactions at these structures are differently coupled with the flow field.

8.3.1 Given Spatial Resolution of Catalyst Structure

In the first case considered, the catalytic layer is resolved in space, that is, the surface of the catalyst is directly exposed to the fluid flow. Examples are thin catalytically coated walls in honeycomb structures, disks, plates, and well-defined porous media (fixed bed reactors, foams, and washcoats), in which the shape of the individual pellet or channel is spatially resolved in the CFD simulation. The chemical processes at the surface are then coupled with the surrounding flow field by boundary conditions for the species continuity equation (8.4) at the gas–surface interface [2, 28]:

$$\vec{n}(\vec{j}_i + \varrho \vec{v}_{\text{Stef}} Y_i) = R_i^{\text{het}}. \tag{8.14}$$

Here, $\vec{n}$ is the outward-pointing unit vector normal to the surface, $\vec{j}_i$ is the diffusion mass flux of species i as discussed in Eq. (8.4), and R_i^{het} is the heterogeneous surface reaction rate, which is given per unit geometric surface area, corresponding to the reactor geometry, in kg/(m^2 s). Approaches to model the heterogeneous reaction rates R_i^{het} are discussed in Chapter 4 of this book.

The Stefan velocity $\vec{v}_{\text{Stef}}$ occurs at the surface if there is a net mass flux between the surface and the gas phase:

$$\vec{n}\vec{v}_{\text{Stef}} = \frac{1}{\varrho}\sum_{i=1}^{N_g} R_i^{\text{het}}. \tag{8.15}$$

Under steady-state conditions, this mass flux vanishes unless mass is deposited on the surface, for example, chemical vapor deposition, or ablated, for example, material etching. Equation (8.14) basically means that for $\vec{v}_{\mathrm{Stef}} = 0$ the amount of gas-phase molecules of species i, which are consumed/produced at the catalyst by adsorption/desorption, have to diffuse to/from the catalytic wall (Eq. (8.5)). Only for fast transient ($<10^{-4}$ s) adsorption/desorption processes, for example, during ignition of catalytic oxidation, does Eq. (8.14) break down and special treatment of the coupling is needed [29, 30]. In that case, accumulation of species in the near-catalyst zone has to be considered, for example, through [29]

$$\int \varrho \frac{\partial Y_i}{\partial t} \mathrm{d}V = -\int (\vec{j}_i + \varrho \vec{v}_{\mathrm{Stef}} Y_i)\vec{n}\mathrm{d}A + \int R_i^{\mathrm{het}} \mathrm{d}A. \tag{8.16}$$

In that case, special care has to be taken in the spatial discretization procedure [2]. Furthermore, those fast transient processes may lead to heat accumulation terms [29] and to additional convective transport and associated pressure gradients in the fluid phase above the catalyst [30].

Calculation of R_i^{het} is straightforward if the catalytic surface corresponds to the geometrical surface of the fluid–solid interphase of the flow field simulation, for example, wires and flat plates without any porosity. In that case, R_i^{het} is the production rate of species i per *catalyst surface area* due to catalytic reactions (Chapter 4). It should be noted that the catalyst surface area is the surface area (layer on which we find adsorbed species) of the catalytic particle exposed to the ambient gas (fluid) phase, which can be measured, for example, by chemisorptions with sample molecules such as CO and hydrogen. The catalyst surface area should not be confused with the BET surface area.

8.3.2
Simple Approach for Modeling the Catalyst Structure

Most catalytic systems, however, exhibit a certain structure, for instance, they may occur as dispersed particles on a flat or in a porous substrate. The simplest way to account for that structure and the active catalytic surface area consists in scaling the intrinsic reaction rate at the fluid–solid interphase by two parameters. The first parameter represents the amount of catalytically active surface area in relation to the geometric surface area of the fluid–solid interphase, here denoted by $F_{\mathrm{cat/geo}}$:

$$R_i^{\mathrm{het}} = \eta F_{\mathrm{cat/geo}} M_i \dot{s}_i. \tag{8.17}$$

Here, $\dot{s}_i$ is the molar net production rate of gas-phase species i, given in mol/(m^2 s); the area now refers to the actual catalytically active surface area. $F_{\mathrm{cat/geo}}$ can be consequently determined experimentally, for example, by chemisorption measurements. Recently, it was shown that this ratio ($F_{\mathrm{cat/geo}}$) can also serve as parameter to describe the dependence of the overall reaction rate of catalyst loadings and effects of hydrothermal aging for structure-insensitive catalysts [31]. This concept was even applied to model the variation in performance of on-road aged three-way catalysts [32].

The simplest model to include the effect of internal mass transfer resistance for catalysts dispersed in a porous media is the effectiveness factor η based on the Thiele modulus [5, 33]. The effectiveness factor of species i, η_i, is defined as

$$\eta_i = \frac{\dot{s}_{i,\text{mean}}}{\dot{s}_i}, \tag{8.18}$$

with $\dot{s}_{i,\text{mean}}$ as mean surface reaction rate in the porous structure. Assuming a homogeneous porous medium, time-independent concentration profiles, and a rate law of first order, the effectiveness factor can be analytically calculated in terms of

$$\eta_i = \frac{\tanh(\Phi_i)}{\Phi_i}, \tag{8.19}$$

with Φ_i as Thiele module defined as

$$\Phi_i = L\sqrt{\frac{\dot{s}_i\gamma}{D_{\text{eff},i}c_{i,0}}}. \tag{8.20}$$

Here, L is the thickness of the porous medium (washcoat), γ is the ratio of catalytic active surface area to washcoat volume, and $c_{i,0}$ are the species concentrations at the fluid/porous media interface. The Thiele module is a dimensionless number. The value in the root term of Eq. (8.20) represents the ratio of intrinsic reaction rate to diffusive mass transport in the porous structure. Since mass conservation has to be obeyed (Eq. (8.17)), the same effectiveness factor has to be applied for all chemical species. Therefore, this simple model can be applied only under conditions at which the reaction rate of one species determines overall reactivity. Furthermore, this model then implies that mass diffusion inside the porous media can be described by the same diffusion coefficient for all species.

In most fixed bed reactors with large numbers of catalytic pellets, both for nontrivial shapes of the catalysts and for catalyst dispersed in porous media, the structure of the catalyst cannot be resolved geometrically. In these cases, the catalytic reaction rate is expressed per volumetric unit, which means R_i^{het} is now given in kg/(m^3 s); the volume here refers to the volume of a computational cell in the geometrical domain of fluid flow. Then R_i^{het} simply represents an additional source term on the right side of the species continuity equation(8.4) and is computed by

$$R_i^{\text{het}} = \eta S_V M_i \dot{s}_i, \tag{8.21}$$

where S_V is the active catalytic surface area per volumetric unit, given in m^{-1}, determined experimentally or estimated. Both $F_{\text{cat/geo}}$ and S_V can be expressed as function of the reactor position and time to account for inhomogeneously distributed catalysts and loss of activity, respectively. In reactors with more than one catalytic material, a different value for $F_{\text{cat/geo}}$ or S_V can be given for every individual active material or phase, respectively.

8.3.3
Reaction Diffusion Equations

The dispersion of the catalyst material in porous layers or pellets easily leads to a reduced overall reaction rate due to finite diffusion of the reactants to and products from the active sites. The simplest model to account for this mass transport limitation is the effectiveness factor η as introduced above. However, this model fails under conditions in which the reaction rate and diffusion coefficient of more than a single species determine overall reactivity. Like in this case, the interaction of diffusion and reaction demands more detailed models if mass transport in the porous media is dominated rather by diffusion than by convection.

Concentration gradients inside the porous media result in spatial variations in the surface reaction rates $\dot{s}_i$. In thin catalyst layers (washcoats), these are primarily significant in normal direction to the fluid/washcoat boundary. Therefore, one-dimensional reaction diffusion equations are applied with their spatial coordinate in that direction. Each chemical species leads to one reaction diffusion equation, which is written in steady state as

$$\frac{\partial}{\partial r}\left(-D_i^{\mathrm{eff}}\frac{\partial c_i^{\mathrm{W}}}{\partial r}\right)-S_{\mathrm{V}}\dot{s}_i = 0. \tag{8.22}$$

Here, c_i^{W} denotes the species concentration in the washcoat in normal direction to the boundary fluid/washcoat. D_i^{eff} is the effective diffusion coefficient, which can account for the different diffusion processes in macro- and micropores and can be derived from the binary diffusion coefficients [23, 34]. In addition to Eq. (8.22), the surface coverages can be calculated, assuming a *microkinetics* model is available, according to

$$\frac{\mathrm{d}\theta_i}{\mathrm{d}t} = \frac{\dot{s}_i\sigma_i}{\Gamma}. \tag{8.23}$$

A heat balance, in which Eqs. (8.7) and (8.10) are combined, may be added to the model to account for temperature variations in the porous media. Since Eq. (8.22) is applicable only for thin catalytic layers or small pellets without net mass fluxes (ablation, deposition, etc.) and internal pressure-driven flows, temperature variations can generally be neglected. Equation (8.22) is coupled with the surrounding flow field, Eq. (8.5), at the interface between open fluid and catalytic layer/pellet, where the diffusion fluxes normal to this interface must compensate. In this model, the species concentrations, catalytic reaction rates, and surface coverages do not only depend on the position of the catalytic layer/pellet in the reactor but also vary inside the catalyst layer/particle leading to CPU time-consuming computations.

8.3.4 Dusty Gas Model

Fluxes within porous media that are driven by gradients in concentration and pressure, that is, diffusion and convection, can be described by the dusty gas model (DGM) [23, 34]. This model, which is also applicable for three-dimensional and larger porous media, not only is superior to the ones discussed in the previous two sections but also leads to more sophisticated computational efforts. The conservation equation (8.4) for reactive porous media species transport at steady state is now written as

$$\frac{\partial(j_{i,j})}{\partial x_j} = R_i^{\mathrm{hom}} + R_i^{\mathrm{het}} = R_i^{\mathrm{hom}} + S_{\mathrm{V}} M_i \dot{s}_i. \tag{8.24}$$

The components j of the gas-phase mass fluxes, $j_{i,j}$, of species i are evaluated by an implicit relationship among the molar concentrations, concentration gradients, and pressure gradients [23, 34]:

$$j_{i,j} = \left[-\sum_{l=1}^{N_{\mathrm{g}}} D_{il}^{\mathrm{DGM}} \frac{\partial c_l}{\partial x_j} - \left(\sum_{l=1}^{N_{\mathrm{g}}} D_{il}^{\mathrm{DGM}} \frac{c_l}{D_{l,\mathrm{Kn}}^{\mathrm{eff}}} \right) \frac{\alpha}{\mu} \frac{\partial p}{\partial x_j} \right] M_i. \tag{8.25}$$

Here, D_{il}^{DGM} are the DGM diffusion coefficients and $D_{i,\mathrm{Kn}}^{\mathrm{eff}}$ are the effective Knudsen diffusion coefficients. The first term on the right-hand side of Eq. (8.25) represents the diffusive flux and the second the viscous flux. The DGM diffusion coefficients can be represented as a matrix inverse $D_{il}^{\mathrm{DGM}} = H^{-1}$, where the elements of the H matrix are given by

$$h_{il} = \left[\frac{1}{D_{i,\mathrm{Kn}}^{\mathrm{eff}}} + \sum_{j \neq i} \frac{X_j}{D_{ij}^{\mathrm{eff}}} \right] \delta_{il} + (\delta_{il} - 1) \frac{X_j}{D_{il}^{\mathrm{eff}}}. \tag{8.26}$$

The effective binary diffusion coefficients D_{il}^{eff} in the porous media are related to the ordinary binary diffusion coefficient D_{il} by

$$D_{il}^{\mathrm{eff}} = \frac{\Phi_{\mathrm{g}}}{\tau_{\mathrm{g}}} D_{il}, \tag{8.27}$$

with Φ_{g} = porosity and τ_{g} = tortuosity. The effective Knudsen diffusion coefficient can be expressed as

$$D_{i,\mathrm{Kn}}^{\mathrm{eff}} = \frac{2}{3} \frac{\Phi_{\mathrm{g}}}{\tau_{\mathrm{g}}} r_{\mathrm{p}} \sqrt{\frac{8RT}{\pi M_i}}, \tag{8.28}$$

where r_{p} is the average pore radius.

A critical evaluation of transport models including DGM and the development of a more general concept have been proposed by Kerkhof [35, 36]. For more on transport in porous media in interaction with catalytic reactions, the reader may refer to Chapters 5 and 6.

8.4
Numerical Methods and Computational Tools

There are a variety of methods to solve the coupled system of partial differential equations (PDE) and algebraic equations, which were presented in the previous sections for modeling catalytic reactors. Very often, the transient three-dimensional governing equations are simplified (no time dependence, symmetry, preferential flow direction, infinite diffusion, etc.) as much as possible, but still taking care of all significant processes in the reactor. Simplifications often are not straightforward and need to be conducted with care. Special algorithms were developed for special types of reactors to achieve a converged solution or to speed up the computation.

8.4.1 Numerical Methods for the Solution of the Governing Equations

An analytical solution of the PDE system is possible only in very limited special cases; for all practical cases, a numerical solution is needed. Numerical solution means that algebraic equations are derived that approximate the solution of the PDE system at discrete points of the geometrical space of the reactor. The way of selection of these grid points and the derivation of algebraic equations, which are finally solved by the computer, is called discretization. Since the solution of the discretized equations is only an approximation of the solution of the PDE system, an error analysis is an essential feature of the interpretation of every CFD simulation.

The three major methods of discretization [37] are the methods of finite differences (FDM), finite volumes (FVM), and finite elements (FEM). The simplest method is FDM, which is based on a Taylor series expansion of the solution vector between neighboring grid points and applied for well-structured grids. The chosen number of terms of the Taylor series determines the accuracy. In contrast to FDM, the finite volume method can be applied for unstructured grids so that for regions with larger gradients more grid points can be chosen, well adapted to the reactor behavior. FVM calculates the dependent variables not for certain points but for certain volumes. Source terms within cells and fluxes through the boundaries of these cells are considered to derive the local values, which not only makes this method very physically descriptive but also allows simple error estimation.

The most universal method from a mathematical point of view is FEM [38, 39]; FDM and FVM can be considered as special cases of FEM. FEM originates from structural mechanics and has meanwhile found increased use in CFD. FEM generates the computational grid in a very adaptive way and is therefore ideal for complex geometries. Furthermore, FEM-based codes are suitable for the application of parallel computing. The great flexibility of FEM regarding the description of the solution and its convergence comes at the cost of a higher complexity of the computer program. Today, all commercial CFD codes are based on either FVM or FEM.

Very different from these three methods are the lattice–Boltzmann methods (LBMs) [40], which have become popular in particular for the simulation of complex flow structures found in fixed beds [41–43]. The LBM may be considered as a finite difference method for a discrete Boltzmann equation. The method simulates hydrodynamic or mass transport phenomena by tracking the time evolution of particle distribution functions confined to a lattice moving with discrete velocity during discrete advances in time. Each time step is subdivided into separate streaming and collision steps. It could be shown that correctly chosen particle distribution functions recover the Navier–Stokes equations. LBM for reaction engineering applications is still under development; in particular, the implementation of heat transport and complex reaction schemes seems to be difficult. There is no commercial code based on LBM available yet.

8.4.2
CFD Software

Available multipurpose commercial CFD codes can simulate very complex flow configurations including turbulence and multicomponent transport based on FVM and FEM. However, CFD codes still have difficulties to implement complex models for the chemical processes. One problem is the insufficient number of reactions and species the codes can handle. An area of recent development is the implementation of detailed models for heterogeneous reactions.

Several software packages have been developed for modeling complex reaction kinetics in CFD such as CHEMKIN [44], CANTERA [45], DETCHEM [46], which also offer CFD codes for special reactor configurations such as channel flows and monolithic reactors. These kinetic packages and also a variety of user written subroutines for modeling complex reaction kinetics have meanwhile been coupled to several commercial CFD codes. Aside from the commercially widespread multipurpose CFD software packages such as ANSYS FLUENT [47], STAR-CD [48], FIRE [49], CFD-ACE + [50], CFX [51], a variety of multipurpose and specialized CFD codes have been developed in academia and at research facilities such as MP-SALSA [52]. The latter ones are often customized for special reactor types and therefore more efficient. Another tool for the solution of PDE systems based on the finite element method is the FEMLAB software package [53], which has been applied for CFD simulations of catalytic reactors as well. Recently, the free, open source CFD software package OpenFOAM (OpenCFD Ltd) gained popoularity.

8.4.3
Solvers for Stiff ODE and DAE Systems

Model simplification and numerical algorithms make it possible to convert the PDE system of the governing equations to an ordinary differential equation (ODE) system or a coupled system of ODEs and algebraic equations called differential algebraic equation (DAE) system. In these equation systems, time or one spatial component is the independent variable. Several computer codes have been developed to solve ODE and DAE systems. In particular, suitable for reactive flows are DASSL [54], LSODE [55], LIMEX [56, 57], SUNDIALS from LLNL, and VODE [58], which are written in FORTRAN language. *The Trilinos Project* [59] offers ODE and DAE solvers written in C programming language. For the underlying theory of the numerical solution of DAE systems and software implementation, one can refer to the textbook by Ascher and Petzold [60].

8.5
Reactor Simulations

In the remainder of this chapter, recent and challenging CFD simulations of catalytic reactors will be discussed according to the type of reactor.

8.5.1 Flow through Channels

There is a wide variety of chemical reactors, in which the reactive mixtures flow trough channel-like devices such as tubular chemical reactors, automotive catalytic converters, and catalytic combustion monoliths.

Pipes with diameters ranging from a few centimeters to meters are one class of those reactors. The flow field here is in most cases turbulent, guaranteeing good mixing of the reactants. A fine resolution of flow field details is rarely of interest, and aside from that, such a task exceeds today's computer capacities. Therefore, averaged equations and turbulence models are applied as discussed above.

Mantzaras *et al.* [15] applied the k–ε model, a presumed (Gaussian) probability density function for gaseous reactions, and a laminar-like closure for surface reactions to study turbulent catalytically stabilized combustion of lean hydrogen–air mixtures in plane platinum-coated channels. They also examined different low-Reynolds number near-wall turbulence models and compared the numerically predicted results with data derived from planar laser-induced fluorescence measurements of OH radicals, Raman measurements of major species, and laser doppler velocimetry measurements of local velocities and turbulence [61]. They found that discrepancies between predictions and measurements are ascribed to the capacity of the various turbulence models to capture the strong flow laminarization induced by heat transfer from the hot catalytic surfaces. A more detailed discussion on laminar and turbulent flows in catalytically coated channels can be found in Chapter 7.

Another class of tube-like reactors is the monolith or honeycomb structure, which consists of numerous passageways with diameters reaching from one-tenth of a millimeter to few millimeters. The flow field in the thin channels of this reactor type is usually laminar. The catalytic material is mostly dispersed in a washcoat on the inner channel wall. Monolith channels are manufactured with various cross-sectional shapes, for example, circular, hexagonal, square, or sinusoidal. Several recent CFD studies were conducted to understand the impact of the real washcoat shape on transport and overall reaction rate [33, 62, 63]. Hayes *et al.* [63] recently showed for a catalytic structure used for exhaust gas cleanup in automobiles that the internal diffusion resistance, expressed in terms of an effectiveness factor, cannot be represented in terms of a unique curve using the generalized Thiele modulus approach to model diffusion and reaction in the washcoat of a catalytic monolith reactor. The most significant deviation occurs when the washcoat has the greatest variation in thickness. As shown in Figure 8.2, only a thin layer of the washcoat in the corners of the channel is needed for conversion, which implies that the corners can be coated with a catalyst-free layer to reduce the amount of expensive noble metals. Mladenov *et al.* recently coupled the three-dimensional Navier–Stokes equations with washcoat diffusion models and an elementary-step-like heterogeneous reaction mechanism consisting of 74 reactions among 11 gas-phase and 22 adsorbed surface species to study mass transfer in single channels of a honeycomb-type automotive catalytic converter operated under direct oxidation conditions [64]. The resulting concentration profiles (Figure 8.3) at constant temperature were compared with 17

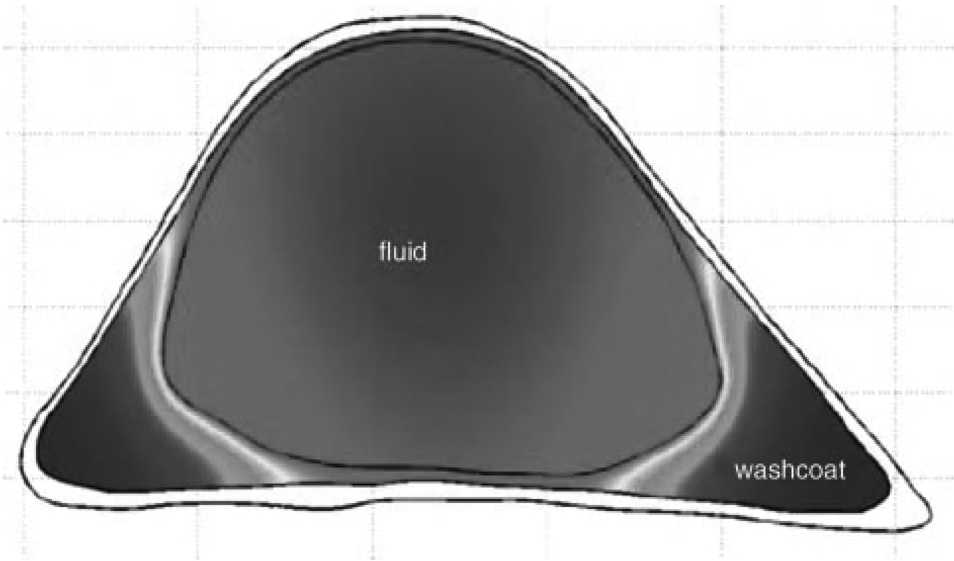

Figure 8.2 Concentrations distribution in the washcoat for a "sinusoidal" channel with highly nonuniform washcoat at 700 K. Adapted from Hayes *et al.* [63].

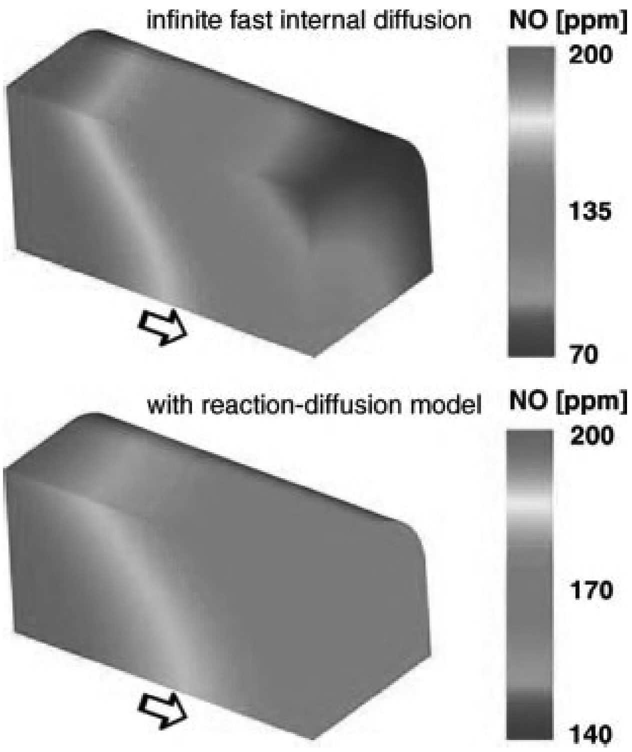

Figure 8.3 Comparison of the NO concentration profiles in a single channel of a honeycomb-type automotive catalytic converter operated under direct oxidation conditions at 250 °C. 3D Navier–Stokes simulation with infinite fast diffusion in the washcoat (*top*) and detailed reaction-diffusion model to describe the internal mass transport. The arrows at the symmetry axes show the main flow direction. Adapted from Mladenov *et al.* [64].

different numerical models with increasingly simplifying models concerning channel cross section and external and internal diffusion. Again, internal diffusion in the washcoat determines overall activity. Even heat balances also accounting for heat conducting channel walls and external heat loss were coupled with the three-dimensional Navier–Stokes equations including detailed reaction mechanisms for the simulation of partial oxidation of methane to synthesis gas on rhodium-coated monoliths with a rectangular channel cross section [65]. On this level, computing time easily increases to several hours.

Since those 3D simulations require long computing times, the single channel is often approximated by a perfect cylindrical geometry, even for noncircular cross sections. Furthermore, the inlet flow pattern is assumed to follow this geometry. Hence, the flow through the single channel can be treated as the flow through a tubular reactor that means two dimensional (2D) with the axial and radial position as independent variables. The resulting 2D Navier–Stokes equations still describe an elliptic flow; that means information in the channel may travel not only downstream but also upstream, which makes the numerical solution still expensive. As the flow rate in the channel increases (i.e., high Reynolds number but still laminar), the axial diffusive transport is diminished in comparison to the radial diffusion and the convective transport. Hence, all the second derivatives in axial direction can be eliminated in Eqs. (8.2), (8.4) and (8.7) [2, 66, 67]. Mathematically, the character of the equations is changed from elliptic to parabolic – a huge simplification, leading to a much more efficient computational solution. This well-known simplification is generally known as the boundary layer approximation, which is widely used in fluid mechanics. The boundary layer equations form a DAE system, with the time-like direction being the axial coordinate. These simplifications now permit the coupling of the flow field simulation with even very large reaction mechanisms. In terms of these assumptions, the catalytic partial oxidation of the gasoline surrogate *iso*-octane over a Rh-coated monolith was studied in terms of complex reaction mechanisms consisting of 7193 homogeneous and 58 heterogeneous reactions among 857 gas phase and 17 surface species [68]. This detailed description led to the explanation of the experimentally observed coke formation in the downstream section of the catalyst. As Figure 8.4 reveals, the formation of hydrogen is mass transfer limited in the first section of the catalyst, the diffusion of oxygen being the rate-limiting process. The very low oxygen concentration at the catalytic channel wall leads to some formation of hydrogen in a region where the oxygen concentration in the gaseous bulk phase is still sufficiently high to promote total oxidation. In general, the reaction sequence is very similar to the behavior observed for light hydrocarbons by many groups [69–73]: after a short initial total oxidation zone leading to steam and CO_2, the oxygen deficiency at the catalytic surface leads to the formation of hydrogen by steam reforming and partial oxidation. Due to the high temperature of approximately 1000 °C, some remaining fuel is pyrolyzed by gas-phase reactions to form the coke precursors ethylene and propylene (Figure 8.4), a relatively slow process that is kinetically controlled but presenting a threat to any downstream system such as fuel cell devices [74–76].

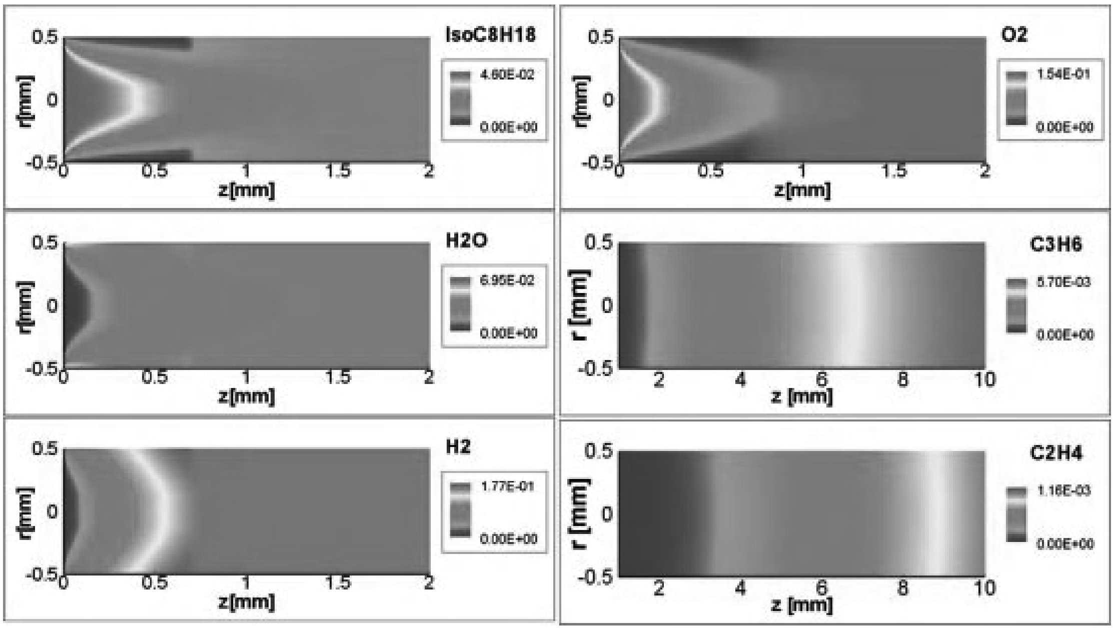

Figure 8.4 Catalytic partial oxidation of *iso*-octane in Rh-coated monolithic channels at C/O = 1.2 and 800 °C. Numerically predicted molar fractions of reactants, hydrogen, water (all for the initial section of 2 mm), and the coke precursors propylene and ethylene (along the entire catalyst of 1 cm). Flow direction is from left to right. Adapted from Hartmann *et al.* [68].

A further simplification of modeling channel flows consists of the assumption of infinite radial mass transport or at least very fast radial mass transport, leading to vanishing gradients of radial concentration and temperature. There is a large amount of literature discussing this so-called plug flow reactor (PFR) model [5], which has been the model of choice until recently, including a variety of extensions such as mass transfer limitations [77] or two-phase approaches [78]. The application of the PFR model becomes unreliable for systems in which fast catalytic reactions [67] and/or homogeneous gas-phase reactions occur [79].

Further detailed simulations were carried out, for instance, by Hayes *et al.* [80], who developed a 2D finite-element model for simulation of a single channel of honeycomb-type monolith catalytic reactor; and Wanker *et al.* [81] conducted transient two-dimensional simulations of a single channel of a catalytic combustor, taking into account the effects occurring in the gas phase, in the washcoat layer, and in the substrate. They also applied their model to simulate a wood-fired domestic boiler [82].

8.5.2
Monolithic Reactors

The simplest way to model honeycomb-like structures, as shown in Figure 8.1, is based on the assumption that all channels behave essentially alike and therefore only one channel needs to be analyzed. If upstream heat conduction does not matter, parabolic approaches as the boundary layer approximation may be used [67], otherwise an elliptic ansatz is needed [65, 79]; both approaches are discussed above. Heat transfer at the outer boundary of the monolith, spatially varying inlet conditions at the front face of the monolith, and different catalyst coatings will demand models that consider the entire monolithic structure. Since the detailed simulation of every individual channel is usually not tractable, simplifying algorithms are needed [83]. Catalytic monoliths, for instance, have been treated as porous media [84], which can save computational time but can yield unreliable results if the interaction of transport and reactions in the individual channels matters.

Another approach combines the simulation of a representative number of channels with the simulation of the temperature profiles of the solid structure treating the latter one as continuum [85–88]. This approach also is the basis for the computer code DETCHEM^{MONOLITH} [46], which has been applied to model the transient behavior of catalytic monoliths. The code combines a transient three-dimensional simulation of a catalytic monolith with a 2D model of the single-channel flow field based on the boundary layer approximation. It uses detailed models for homogeneous gas-phase chemistry, heterogeneous surface chemistry, and contains models for the description of pore diffusion in washcoats. The numerical structure of the code as sketched in Figure 8.5 is based on the following idea: The residence time of the reactive gas in the monolith channels is much smaller than the unsteadiness of the inlet conditions and the thermal response of the solid monolith structure. Under these assumptions, the timescales of the channel flow are decoupled from the temporal temperature variations of the solid, and the following procedure can be applied: A transient multidimensional heat balance is solved for the monolithic structure including the thermal insulation and reactor walls, which are treated as porous continuum. This simulation of the heat balance provides temperature profiles along the channel walls. At each time step, the reactive flow through a representative number of single

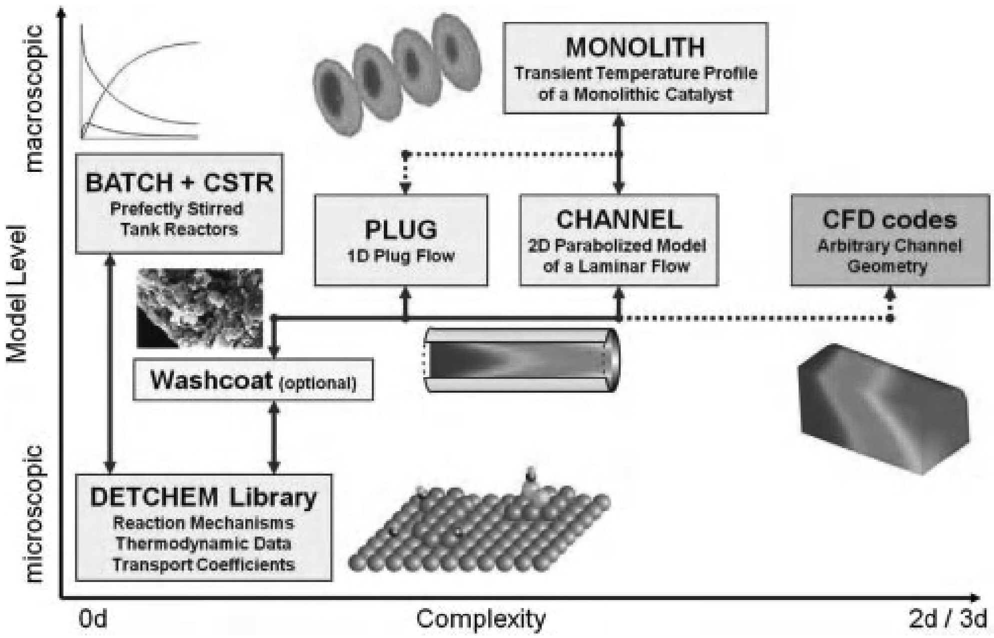

Figure 8.5 Structure of the computer code DETCHEM^{MONOLITH} and some further modules of the software package DETCHEM™ [46].

channels is simulated including detailed transport and chemistry models. These single-channel simulations also calculate the heat flux from the fluid flow to the channel wall due to convective and conductive heat transport in the gaseous flow and heat released by chemical reactions. Thus, at each time step, the single-channel simulations provide the source terms for the heat balance of the monolith structure while the simulation of the heat balance provides the boundary condition (wall temperature) for the single-channel simulations. At each time step, the inlet conditions may vary. This very efficient iterative procedure enables a transient simulation of the entire monolith without sacrificing the details of the transport and chemistry models, as long as the prerequisites for the timescales remain valid. Furthermore, reactors with alternating channel properties such as flow directions, catalyst materials, and loadings can be treated. The code has been applied to model transient behavior of automotive catalytic converters, catalytic combustion monoliths for gas turbine applications, and high-temperature catalysis. Exemplarily, two recently discussed cases are presented as follows:

- In Figure 8.6, the impact of flow rate on the temperature distribution in the monolithic sections of a short-contact time reactor for reforming *iso*-octane to hydrogen-rich synthesis gas reveals that higher flow rates lead to an increase in temperature, conversion, and consequently higher hydrogen yields [89]. This counterintuitive increase in fuel conversion with decreasing residence time

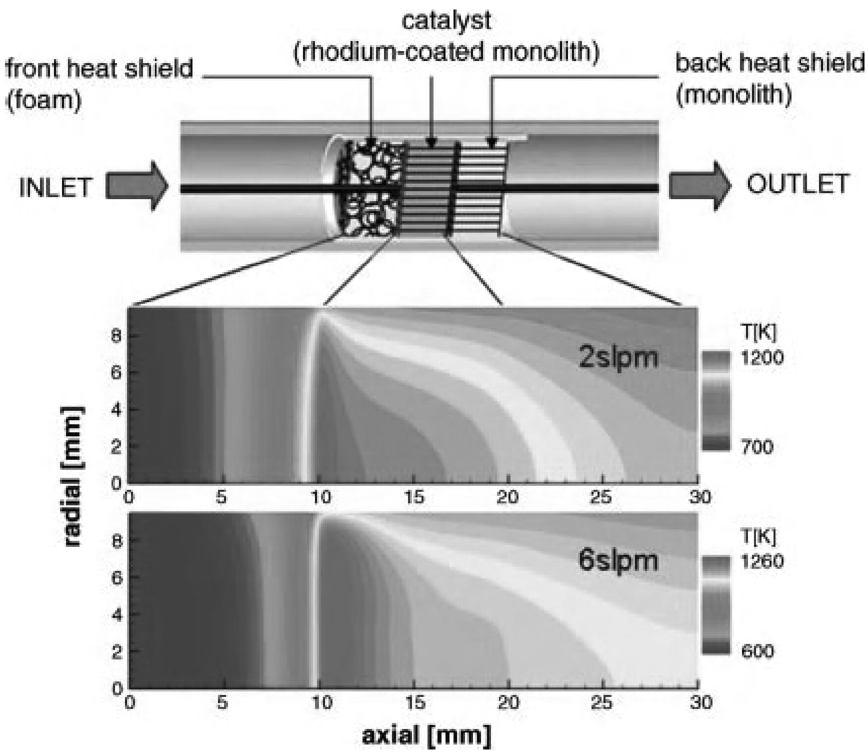

Figure 8.6 Sketch of the catalyst section of a reformer for logistic fuels (*iso*-octane as surrogate) with two heat shields (*top*) and numerically predicted steady-state monolith temperature at C/O = 1.0 and at flow rates of 2 slpm (*top*) and 6 slpm (*bottom*). The symmetry axis of the monolith is at radial dimension of zero. Reproduced from Maier *et al.* [89].

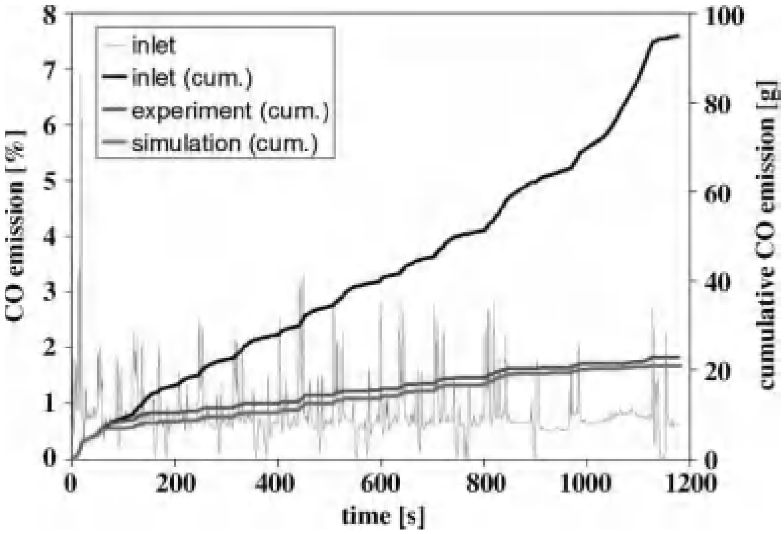

Figure 8.7 Cumulated CO emissions in MVEG driving cycle of an automotive catalytic converter, simulation experiment. The continuously varying raw emissions (inlet, gray color) shown in the background serve as inlet conditions for the simulation. Reproduced from Tischer *et al.* [93].

(increasing flow rate) can be explained by analyzing the ratio of chemical heat release to heat loss in the reactor [90].

- The second example is the simulation of driving cycles to be used by legislation to test automotive catalytic converters. These cycles last about 20 min and cover a very wide range of conditions. Due to spatially varying inlet conditions and radial temperature profiles over the monolithic catalyst structure, a rather large number of channels need to be considered in the simulations [91]. Furthermore, the continuously temporarily varying inlet temperature, exhaust gas composition, and mass flows make such a simulation a formidable task. The code DTECEM$^{\text{MONOLITH}}$ can handle this challenge quite well due to the approach discussed above [92–94]. Figure 8.7 presents a comparison of the experimental and computed time-resolved CO emission in a realistic automobile driving cycle.

8.5.3
Fixed Bed Reactors

The understanding of fluid dynamics and their impact on conversion and selectivity in fixed bed reactors is still very challenging [95, 96]. For large ratios of reactor width to pellet diameter, simple porous media models are usually applicable [97]. This simple approach becomes questionable as this ratio decreases [25, 98]. At small ratios, the individual local arrangement of the particles and the corresponding flow field are significant for mass and heat transfer and, hence, the overall product yields. Therefore, several attempts have recently been made to resolve the flow field in the actual configuration, that is, by a direct numerical simulation (DNS). Even though the governing equations are relatively simple for laminar flows, this approach can be applied usually for small and periodic regions of the reactor only, which is caused by the huge number of computational cells needed to resolve all existing boundary layers [99–105]. Ideally, for simulation of fixed bed reactors, one should account for the transport of chemical species from the bulk of the gas phase to the pellet surface, and then the diffusion and reaction of the species within the catalyst pellets, which may be made up of microporous materials.

Exemplarily, two DNS studies of the group of Dixon will be presented, in which the actual structure of the catalytic fixed bed reactors was taken into account [106–110]. Having spheres as catalyst particles, the modeled turbulent flow and heat transport in a periodic test cell with a tube-to-particle diameter ratio of 4 was simulated [111]. The turbulence was modeled by the renormalization group (RNG) k–ε model [112], and two different wall functions (standard [113] and nonequilibrium) were applied to model the flow field near solid surfaces. Attempts to correlate the local wall heat flux with local properties of the flow field, such as velocity components, velocity gradients, and components of vorticity, led to the conclusion that local heat transfer rates do not correlate statistically with the local flow field. Instead, a conceptual analysis was used to suggest that local patterns of wall heat flux are related to larger-scale flow structures in the bed. Recently, the same group studied the interplay of 3D transport and reaction occurring inside cylindrical pellets and in the gas flow around the pellets used for propane dehydrogenation to better understand catalyst deactivation by carbon deposition (Figure 8.8) [114].

Lattice Boltzmann methods have also been applied for a better understanding of fluid flow in complex reactor configurations [42, 43, 115]. The packing of spheres in cylindrical columns can be created either from experimental observations, such as magnetic resonance imaging (MRI), or by computer simulations. The created topology is then divided into a Cartesian grid, where individual elements are labeled

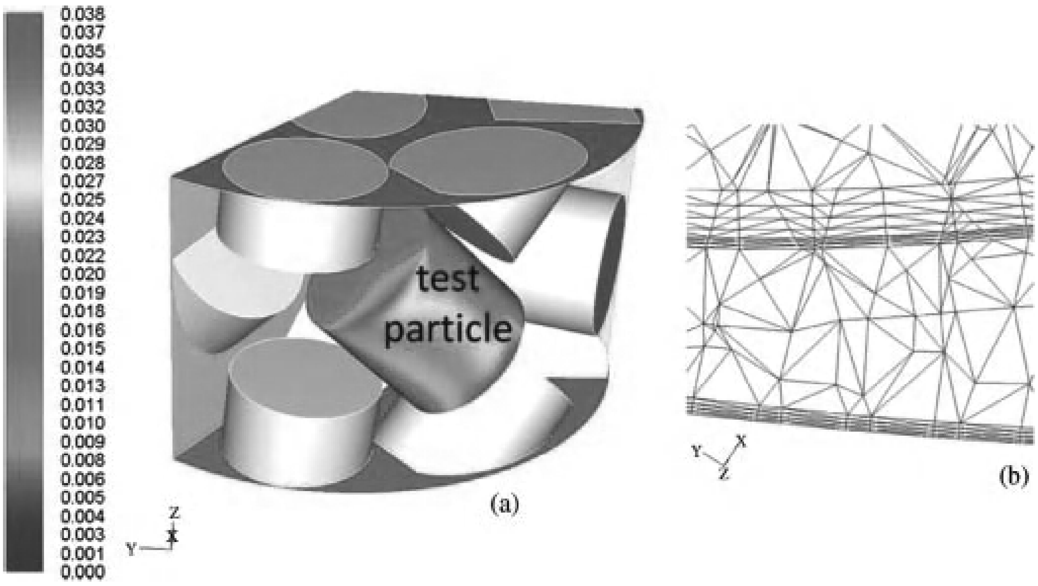

Figure 8.8 Example of a direct numerical simulation of a fixed bed reactor with cylindrical packings showing contours of propane dehydrogenation rate on fresh catalyst (kmol/m^3(solid) s) (a) and details of mesh (b). Reproduced from Dixon *et al.* [114].

as solid or fluid regions. A high resolution of the grid leads to accurate flow profiles. Zeiser *et al.* [43] generated the geometrical structures of the fixed bed with a Monte Carlo method. This allowed to efficiently simulate the placement of randomly packed spheres in a cylinder and to obtain detailed information of statistical properties, such as the distribution of the void fraction. This geometrical information was the basis for subsequent numerical flow simulation using LBM. This approach allowed the prediction of the local fluid velocity distribution in the bed, as well as the transport and rate of simple chemical reactions. Yuen *et al.* [115] studied correlations between local conversion and hydrodynamics in a 3D fixed bed esterification process by applying an LBM and comparing its results with data from *in situ* magnetic resonance visualization techniques.

8.5.4 Wire Gauzes

Wire gauze reactors have been applied for high-temperature catalytic reactions in industry for quite a long time. For example, ammonia is oxidized over Pt/Rh wire gauzes to produce NO (Ostwald process), and similarly, HCN is synthesized by ammoxidation of methane (Andrussov process). Due to the complex 3D geometry, wire gauze reactors have been frequently treated by simpler two-dimensional simulations [116, 117]. However, since mass and heat transport are the dominating processes in wire gauze reactors, simplification of the flow field is risky. Therefore, CFD studies were performed using 3D simulations of the flow field. The 3D flow field through knitted gauzes applied for ammonia oxidation was simulated by Neumann *et al.* [118]. Catalytic partial oxidation (CPOX) of light alkanes was also studied in wire gauze reactors. De Smet *et al.* [119] studied CPOX of methane with oxygen at atmospheric pressure in a continuous flow reactor containing a single Pt metal gauze. They used 3D computations of simultaneous heat and mass transfer in case of a simple surface reaction on the gauze catalyst to derive intrinsic kinetics. This experiment was later simulated using even detailed surface and gas-phase reaction schemes [120]. Figure 8.9 exemplarily shows the computed temperature profile around a Pt/Rh wire gauze used for ammonia oxidation, which was carried out with the commercial CFD code FLUENT [121] coupled with a multistep surface reaction mechanism.

8.5.5 Catalytic Reactors with Multiphase Fluids

CFD simulations have recently been applied to quite a number of catalytic reactor types with multiphase flow fields such as fluidized bed reactors with and without circulation, slurry reactors, trickle bed reactors, membrane reactors, electrocatalytic devices (e.g., fuel cells), and reactive distillation devices. These multiphase reactors are of multiscale structures, that is, single particles, particle clusters/bubbles, and reactor vessel, and of multiple physics, that is, hydrodynamics, heat and mass transfer, and reaction kinetics. The formation of complex structures/patterns in each regime is a result of a compromise between dominant mechanisms at multiple

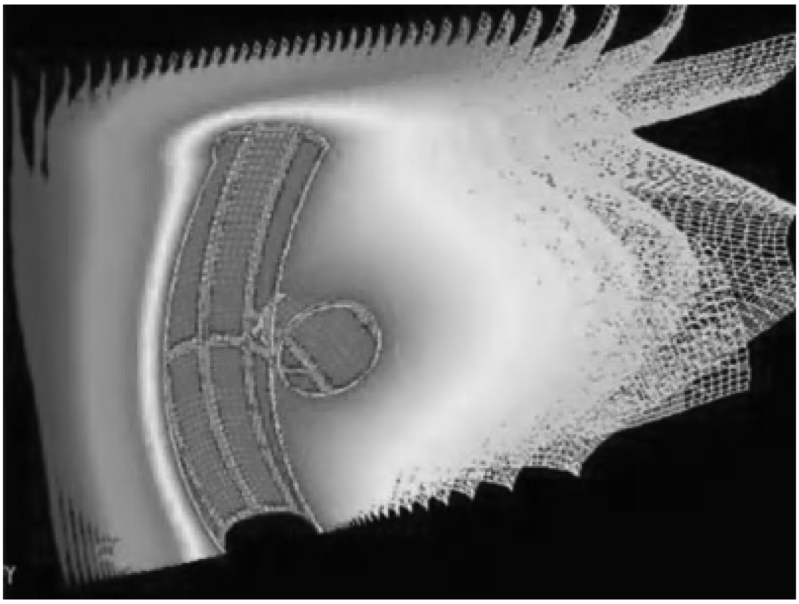

Figure 8.9 Computed temperature profile (max. 950 °C) around a Pt/Rh wire gauze used for ammonia oxidation (Ostwald process).

scales. Coupling of hydrodynamics, heat and mass transfer, and reaction kinetics takes place at molecular and particle levels where conductive and convective transfer and diffusion within the internal pores of the catalyst are accompanied by the adsorption, surface reaction, and desorption of reactant and product on the surface. Even though this complexity is challenging for CFD simulations, computations are a promising tool to achieve a better understanding of multiphase reactors.

A detailed description of the fundamentals and modeling attempts of these multiphase reactors is beyond the scope of this chapter; here, it is referred to general textbooks [19–21]. Instead, few examples may serve as illustration of the potential of CFD simulations of reactors with multiphase flow fields.

Heterogeneously catalyzed gas–liquid reactions, such as hydrogenations, oxidations, hydroformylations, and Fischer–Tropsch synthesis are frequently carried out in slurry reactors. The catalysts of typical diameter of 1–100 μm are suspended in the liquid phase, the injecting gas providing the mixing and catalyst suspension. The advantages of bubble slurry reactors over fixed bed reactors are better temperature control and high reaction rates using small catalyst particles. The Khinast group studied heterogeneously catalyzed reactions close to bubbles using advanced CFD tools [122]. Their study revealed the influence of bubble size and shape and particle properties on selectivity of fast heterogeneously catalyzed gas–liquid reactions. The reaction was shown to occur primarily in the wake of the bubble for fast gas–liquid–solid reactions (Figure 8.10), and is thus dependent only on mixing in this region.

Recently, Fischer–Tropsch synthesis slurry bubble column reactors have been the objective of several modeling studies [123–125]. Troshko and Zdravistch recently conducted a CFD study based on a Eulerian multifluid formulation with both the liquid–catalyst slurry and the syngas bubbles phases [125]. The model includes

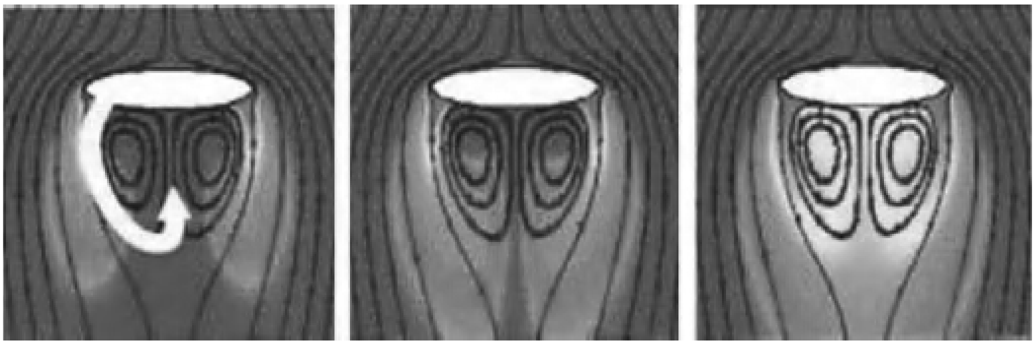

Figure 8.10 Snapshots of the computed developing concentration of the product in the wake of a bubble in a gas–liquid–solid reaction. Reproduced from Raffensberger *et al.* [122]

variable gas bubble size, effects of the catalyst suspended in the liquid phase and chemical reactions. Findings of this study are that the highly localized FT reaction rate appears next to the gas injection region leading to heat release maxima in that region.

The mass and heat transfer in three-phase flow is determined not only by the transport through the interphases but also by convective transport within the bubbles and the liquid structure (Figure 8.11) [126]. Based on a volume-of-fluid method with interface reconstruction computation, bubble shapes were recently computed and experimentally validated in Taylor flows in a viscous liquid within a square channel of 1 mm hydraulic diameter (Figure 8.12) by Wörner and coworkers [127]. These simulations are of great interest for gas–liquid–solid reactions in microstructures, in which the catalyst is dispersed on the solid wall.

8.5.6
Material Synthesis

Chemical reactors for material synthesis are often characterized by interactions between more than one phase, for example, gas phase and solid phase. Chemical vapor deposition (CVD) and chemical vapor infiltration (CVI) are two commonly used methods for material synthesis. The methodology to treat those systems is very close to the one discussed in this book for heterogeneous catalytic reactions and, therefore, a few remarks shall be made.

CVD is widely used for manufacturing thin solid films in semiconductor industry. The complex interactions of a large number of chemical species with flow and heat transport prohibited early CFD models to include detailed chemistry into the reactor models. Nevertheless, for simple configurations such as stagnation flow configuration, codes were developed in the early stage of modeling heterogeneous reactive flows, when Kee and coworkers developed the first tools for CFD modeling of heterogeneous reactions [28, 128, 129]. These tools were applied for catalysis and material synthesis [28, 128, 130, 131]. With increasing computer performance, it became possible to include more detailed descriptions of transport phenomena and reaction chemistry into CFD models. Kleijn [132], for instance, carried out a full 2D

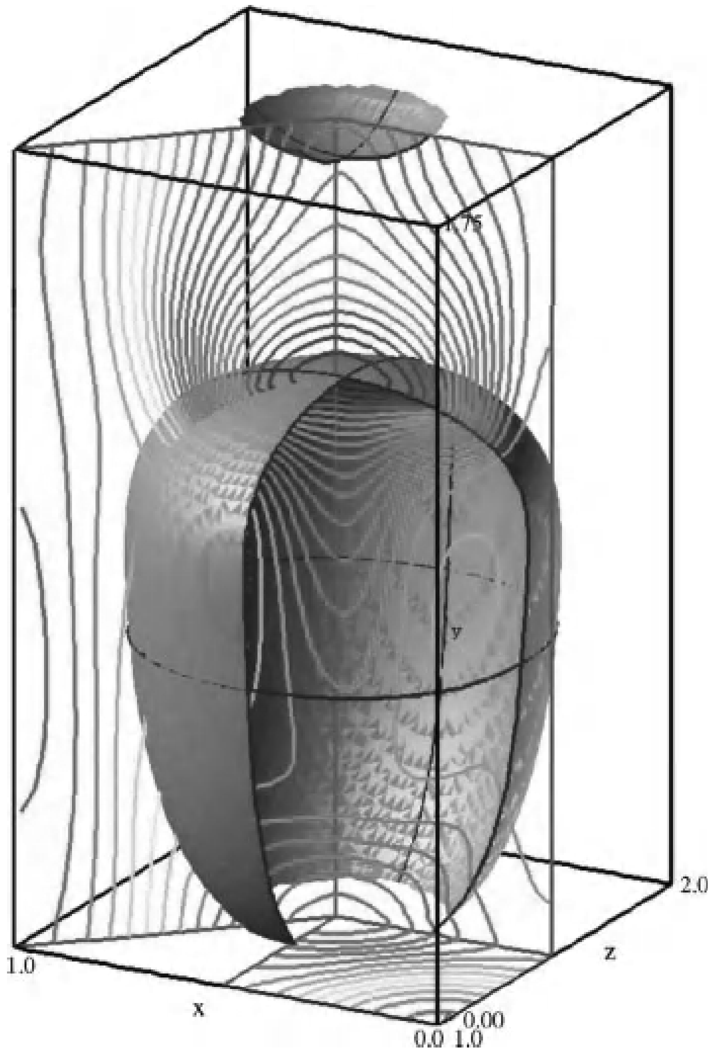

Figure 8.11 Numerical simulation of gas–liquid mass transfer in cocurrent downward Taylor flow; reproduced from Kececi *et al.* [126].

simulation of rotating disk/stagnation flow CVD reactor using CFD models with detailed surface chemistry and could show that properties at the outer edges of the reactor can vary significantly from that of the centerline, especially in the case of stagnation flow.

Modeling CVI is more challenging compared to CVD due to the temporal densification of the porous substrate and hence the changing surface area. These changes significantly influence the interaction between the gas-phase and the surface kinetics. Therefore, one has to incorporate additional model equations that describe the temporal changes in porosity and surface area into the CFD models. Li *et al.* modeled the chemical vapor infiltration (CVI) of hydrocarbons for synthesis of carbon–carbon composites. They coupled the CVI model with COMSOL to simulate the densification of the porous substrate as a function of time [133, 134] and studied the densification of a porous carbon felt using CH_4 precursor. CFD simulations have also found their way into modeling of the synthesis of catalytic particles by flame

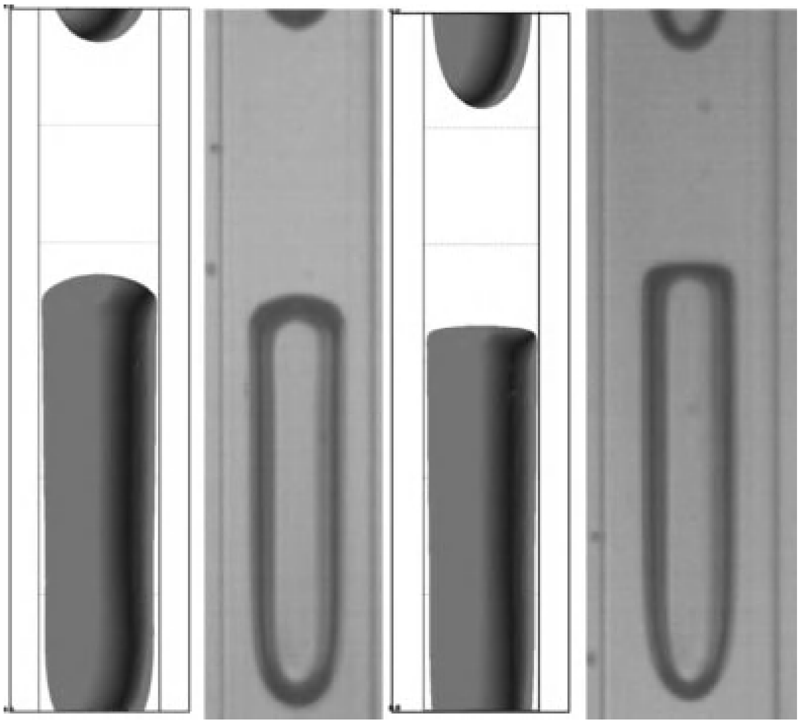

Figure 8.12 Comparison of bubble shape in experiment (*left*) and simulation (*right*) for viscous cocurrent downward Taylor flow in a square minichannel. Reproduced from Keskin *et al.* [127]

synthesis [135], carbon nanotubes [136], and fibrous active materials [137, 138], to name a few more examples related to catalysis.

8.5.7
Electrocatalytic Devices

CFD simulations using heterogeneous reactions are extensively applied to fundamental research pertaining to electrochemical systems, as discussed in more detail for SOFC modeling in Chapter 6. Also, battery dynamics studied using CFD techniques give insightful understanding of its discharge characteristics. Several one-dimensional models are reported in literature that simulate the electrolyte transport and discharge characteristics [139, 140]. Although the one-dimensional models are simple and efficient in predicting the discharge characteristics of battery systems, multidimensional models without any *ad hoc* approximations can be very valuable in the fundamental understanding of processes that occur in battery systems. The ability to visualize flow patterns during operation of a device is a uniqueness of CFD, which is very difficult if not impossible to realize in pure experimentation. Gu *et al.*, for instance, developed a CFD model to predict the transient behavior of electric-vehicle lead acid batteries during charge and discharge processes [141]. The growing interest in lithium ion batteries also led to first CFD applications in this field [142]. CFD simulation has also been used to understand experimentally observed phenomena in electrocatalytic flow cells, in which mass transport interacts with the electric and chemical processes leading to a complex dependence of the Faradaic current on the potential [143].

8.6
Summary and Outlook

From a reaction engineering perspective, computational fluid dynamics simulations have matured into a powerful tool for understanding mass and heat transport in catalytic reactors. Initially, CFD calculations focused on a better understanding of mixing, and mass transfer to enhance reaction rates, diffusion in porous media, and heat transfer. Over the past decade, the flow field and heat transport models have also been coupled with models for heterogeneous chemical reactions. So far, most of these models are based on the mean field approximation, in which the local state of the surface is described by its coverage with adsorbed species averaged on a microscopic scale. The increasing research activities on surface reactions under practical conditions will certainly boost the application of CFD codes that combine fluid flow and chemistry. New insights into the complexity of heterogeneous catalysis, however, will also reveal the demand for more sophisticated chemistry models. Their implementation into CFD simulations will then require even more sophisticated numerical algorithms and computer hardware. Hence, CFD simulations of reactive systems will remain a very active field and the implementation of more adequate and complex models will continue.

The simulation results will always remain a reflection of the models and physical parameters applied. The careful choice of the submodels (geometry, turbulence, diffusion, species, reactions involved, etc.) and the physical parameters (inlet and boundary conditions, conductivity, permeability, viscosity, etc.) is a precondition for reliable simulation results. Therefore, only the use of appropriate models and parameters, which describe all significant processes in the reactor, can lead to reliable results. Furthermore, numerical algorithms never give an accurate solution of the model equations but only an approximated solution. Hence, error estimation is needed. Bearing these crucial issues in mind, CFD can really serve as a powerful tool in understanding the behavior in catalytic reactors and in supporting the design and optimization of reactors and processes.

Acknowledgments

The authors would like to thank R.J. Kee (Colorado School of Mines), S. Tischer, M. Wörner, and L. Maier (all Karlsruhe Institute of Technology) for very stimulating discussions on modeling and simulation of chemical reactors and Y. Dedecek (Karlsruhe Institute of Technology) for editorial corrections of the manuscript. Financial support by the German Research Foundation (DFG) and the Helmholtz Association is gratefully acknowledged.

References

1 Bird, R.B., Stewart, W.E., and Lightfoot, E.N. (2001) *Transport Phenomena*, 2nd edn, John Wiley & Sons, Inc., New York.
2 Kee, R.J., Coltrin, M.E., and Glarborg, P. (2003) *Chemically Reacting Flow*, Wiley-Interscience.
3 Patankar, S.V. (1980) *Numerical Heat Transfer and Fluid Flow*, McGraw-Hill, New York.
4 Warnatz, J., Dibble, R.W., and Maas, U. (1996) *Combustion, Physical and Chemical Fundamentals, Modeling and Simulation, Experiments, Pollutant Formation*, Springer, New York.
5 Hayes, R.E. and Kolaczkowski, S.T. (1997) *Introduction to Catalytic Combustion*, Gordon and Breach Science Publ., Amsterdam.
6 Hirschfelder, J.O., Curtiss, C.F., and Bird, R.B. (1964) *Molecular Theory of Gases and Liquids*, rev. edn, John Wiley & Sons, Inc., New York.
7 Kee, R.J., Dixon-Lewis, G., Warnatz, J., Coltrin, M.E., and Miller, J.A. (1986) A Fortran Computer Code Package for the Evaluation of Gas-Phase Multicomponent Transport Properties, SAND86-8246, Sandia National Laboratories.
8 Chase, M.W., Jr., Davis, C.A., Downey, J.R., Jr., Frurip, D.J., McDonald, R.A., and Syverud, A.N. (1985) *J. Phys. Chem. Ref. Data*, **14**, 1.
9 Kee, R.J., Rupley, F.M., and Miller, J.A. (1987) The Chemkin Thermodynamic Database, SAND87-8215, Sandia National Laboratories, Livermore.
10 Burcat, A. (1984) in *Combustion Chemistry* (ed. W.C. Gardiner), Springer, New York, p. 455.
11 Benson, S.W. (1976) *Thermochemical Kinetics*, John Wiley & Sons, Inc., New York.
12 Libby, P.A. and Williams, F.A. (1993) *Turbulent Reactive Flow*, Academic Press, London.
13 Pope, S.B. (1985) *Prog. Energ. Combust.*, **11**, 119.
14 Appel, C., Mantzaras, J., Schaeren, R., Bombach, R., and Inauen, A. (2005) *Combust. Flame*, **140**, 70.
15 Mantzaras, J., Appel, C., Benz, P., and Dogwiler, U. (2000) *Catal. Today*, **59**, 3.
16 Laudner, B.E. and Spalding, D.B. (1972) *Mathematical Models of Turbulence*, Academic Press, London.
17 Gutheil, E. and Bockhorn, H. (1987) *Physicochem. Hydrodyn.*, **9**, 525.
18 Zhang, X.Y. and Ahmadi, G. (2005) *Chem. Eng. Sci.*, **60**, 5089.
19 Jakobsen, H.A. (2008) *Chemical Reactor Modeling: Multiphase Reactive Flows*, Springer, Heidelberg.
20 Crowe, C.T., Schwarzkopf, J.D., Sommerfeld, M., and Tsuji, Y. (1998) *Multiphase Flows with Droplets and Particles*, CRC Press.
21 Ishii, M. and Hibiki, T. (2006) *Thermo-Fluid Dynamics of Two-Phase Flow*, Springer.
22 Aris, R. (1975) *The Mathematical Theory of Diffusion and Reaction in Permeable Catalysts*, Clarendon Press, Oxford.
23 Keil, F. (1999) *Diffusion und Chemische Reaktionen in der Gas-Feststoff-Katalyse*, Springer, Berlin.
24 Keil, F.J. (2000) *Catal. Today*, **53**, 245.
25 Bey, O. and Eigenberger, G. (1997) *Chem. Eng. Sci.*, **52**, 1365.
26 Giese, M., Rottschafer, K., and Vortmeyer, D. (1998) *Am. Inst. Chem. Eng. J.*, **44**, 484.
27 Winterberg, M., Tsotsas, E., Krischke, A., and Vortmeyer, D. (2000) *Chem. Eng. Sci.*, **55**, 967.
28 Coltrin, M.E., Kee, R.J., and Rupley, F.M. (1991) SURFACE CHEMKIN (Version 4.0): A Fortran Package for Analyzing Heterogeneous Chemical Kinetics at a Solid-Surface–Gas-Phase Interface, SAND91-8003B, Sandia National Laboratories.
29 Deutschmann, O., Schmidt, R., Behrendt, F., and Warnatz, J. (1996) *Proc. Comb. Inst.*, **26** 1747.
30 Raja, L.L., Kee, R.J., and Petzold, L.R. (1998) *Proc. Comb. Inst*, **27** 2249.
31 Boll, W., Tischer, S., and Deutschmann, O. (2010) *Ind. Eng. Chem. Res.*, **49**, 10303.
32 Kang, S.B., Kwon, H.J., Nam, I.S., Song, Y.I., and Oh, S. (2011) *Ind. Eng. Chem. Res.*, **50** 5499.

33 Papadias, D., Edsberg, L., and Björnbom, P.H. (2000) *Catal. Today*, **60**, 11.

34 Mason, E. and Malinauskas, A. (1983) *Gas Transport in Porous Media: The Dusty-Gas Model*, Elsevier, New York.

35 Kerkhof, P. and Geboers, M.A.M. (2005) *Am. Inst. Chem. Eng. J.*, **51**, 79.

36 Kerkhof, P. (1996) *Chem. Eng. J.*, **64**, 319.

37 Ranade, V.V. (2002) *Computational Flow Modeling for Chemical Reactor Engineering*, Acadamic Press.

38 Hayes, R.E., Kolaczkowski, S.T., and Thomas, W.J. (1997) *Comput. Chem. Eng.*, **16**, 654.

39 Burnett, D.S. (1987) *Finite Elemnet Analysis*, Addison-Wesley Publ. Co., Reading.

40 Succi, S. (2001) *The Lattice Boltzmann Equation for Fluid Dynamics and Beyond*, Oxford University Press.

41 Sullivan, S.P., Sani, F.M., Johns, M.L., and Gladden, L.F. (2005) *Chem. Eng. Sci.*, **60**, 3405.

42 Freund, H., Zeiser, T., Huber, F., Klemm, E., Brenner, G., Durst, F., and Emig, G. (2003) *Chem. Eng. Sci.*, **58**, 903.

43 Zeiser, T., Lammers, P., Klemm, E., Li, Y.W., Bernsdorf, J., and Brenner, G. (2001) *Chem. Eng. Sci.*, **56**, 1697.

44 Kee, R.J., Rupley, F.M., Miller, J.A., Coltrin, M.E., Grcar, J.F., Meeks, E., Moffat, H.K., Lutz, A.E., Dixon-Lewis, G., Smooke, M.D., Warnatz, J., Evans, G.H., Larson, R.S., Mitchell, R.E., Petzold, L.R., Reynolds, W.C., Caracotsios, M., Stewart, W.E., Glarborg, P., Wang, C., and Adigun, O. (2000.) *CHEMKIN*, 3.6 edn, Reaction Design, Inc., San Diego, www.chemkin.com.

45 Goodwin, D.G. (2003) CANTERA. An open-source, extensible software suite for CVD process simulation, www.cantera.org.

46 Deutschmann, O., Tischer, S., Correa, C., Chatterjee, D., Kleditzsch, S., and Janardhanan, V.M. (2004) Detchem Software Package, 2.0 edn, Karlsruhe, www.detchem.com.

47 (2005). FLUENT, Fluent Incorporated, Lebanon, www.fluent.com.

48 in CD-adapco, London Office, 200 Shepherds Bush Road, London, W6 7NY, United Kingdom, www.cd-adapco.com.

49 (2005) FIRE, AVL LIST GmbH, Graz, Austria, www.avl.com.

50 (2005) CFD-AC+, CFD Research Corporation, Huntsville, AL, www.cfdrc.com.

51 (2005). CFX, www-waterloo.ansys.com.

52 Shadid, J., Hutchinson, S., Hennigan, G., Moffat, H., Devine, K., and Salinger, A.G. (1997) *Parallel Comput.*, **23**, 1307.

53 (2005) FEMLAB, www.comsol.com.

54 Brenan, K.E., Campbell, S.L., and Petzold, L.R. (1996) *Numerical Solution of Initial-Value Problems in Differential-Algebraic Equations*, 2nd edn, SIAM, Philadelphia, PA.

55 Hindmarsh, A.C. (1983) *Scientific Computing* (ed. R.S. Stepleman), North Holland Publishing Co., Amsterdam, p. 55.

56 Deuflhardt, P., Hairer, E., and Zugk, J. (1987) *Numer. Math.*, **51**, 501.

57 Deuflhard, P. and Nowak, U. (1987) *Progr. Sci. Comput.*, **7**, 37.

58 Brown, P.N., Byrne, G.D., and Hindmarsh, A.C. (1989) *SIAM J. Sci. Statist. Comput.*, **10**, 1038.

59 (2011) The Trilinos Project, Sandia National Laboratories, http://trilinos.sandia.gov/.

60 Ascher, U.M. and Petzold, L.R. (1998) *Computer Methods for Ordinary Differential Equations and Differential-Algebraic Equations*, SIAM, Philadelphia, PA.

61 Appel, C., Mantzaras, J., Schaeren, R., Bombach, R., Kaeppeli, B., and Inauen, A. (2003) *Proc. Comb. Inst.*, **29**, 1031.

62 Hayes, R.E., Liu, B., and Votsmeier, M. (2005) *Chem. Eng. Sci.*, **60**, 2037.

63 Hayes, R.E., Liu, B., Moxom, R., and Votsmeier, M. (2004) *Chem. Eng. Sci.*, **59**, 3169.

64 Mladenov, N., Koop, J., Tischer, S., and Deutschmann, O. (2010) *Chem. Eng. Sci.*, **65**, 812.

65 Deutschmann, O., Schwiedernoch, R., Maier, L., and Chatterjee, D. (2001) *Natural Gas Conversion VI, Studies in Surface Science and Catalysis*, vol. 136

(eds E. Iglesia, J.J. Spivey, and T.H. Fleisch), Elsevier, Alaska, p. 251.
66 Schlichting, H. and Gersten, K. (1999) *Boundary-Layer Theory*, 8th edn, Springer, Heidelberg.
67 Raja, L.L., Kee, R.J., Deutschmann, O., Warnatz, J., and Schmidt, L.D. (2000) *Catal. Today*, **59**, 47.
68 Hartmann, M., Maier, L., Minh, H.D., and Deutschmann, O. (2010) *Combust. Flame*, **157**, 1771.
69 Schwiedernoch, R., Tischer, S., Correa, C., and Deutschmann, O. (2003) *Chem. Eng. Sci.*, **58**, 633.
70 Karagiannidis, S., Mantzaras, J., Jackson, G., and Boulouchos, K. (2007) *Proc. Comb. Inst.*, **31**, 3309.
71 Maestri, M., Vlachos, D.G., Beretta, A., Forzatti, P., Groppi, G., and Tronconi, E. (2009) *Top. Catal.*, **52**, 1983.
72 Beretta, A., Groppi, G., Lualdi, M., Tavazzi, I., and Forzatti, P. (2009) *Ind. Eng. Chem. Res.*, **48**, 3825.
73 Horn, R., Degenstein, N.J., Williams, K.A., and Schmidt, L.D. (2006) *Catal. Lett.*, **110**, 169.
74 Hartmann, M., Kaltschmitt, T., and Deutschmann, O. (2009) *Catal. Today*, **147**, S204.
75 Hebben, N., Diehm, C., and Deutschmann, O. (2010) *Appl. Catal. A Gen.* **2010**, *388*, 225
76 Kaltschmitt, T., Maier, L., and Deutschmann, O. (2010) *Proc. Comb. Inst.*, **33**, 3177.
77 Hayes, R.E. and Kolaczkowski, S.T. (1999) *Catal. Today*, **47**, 295.
78 Veser, G. and Frauhammer, J. (2000) *Chem. Eng. Sci.*, **55**, 2271.
79 Zerkle, D.K., Allendorf, M.D., Wolf, M., and Deutschmann, O. (2000) *J. Catal.*, **196**, 18.
80 Hayes, R.E., Kolaczkowski, S.T., and Thomas, W.J. (1992) *Comput. Chem. Eng.*, **16**, 645.
81 Wanker, R., Raupenstrauch, H., and Staudinger, G. (2000) *Chem. Eng. Sci.*, **55**, 4709.
82 Wanker, R., Berg, M., Raupenstrauch, H., and Staudinger, G. (2000) *Chem. Eng. Technol.*, **23**, 535.
83 Kolaczkowski, S.T. (1999) *Catal. Today*, **47**, 209.
84 Mazumder, S. and Sengupta, D. (2002) *Combust. Flame*, **131**, 85.
85 Jahn, R., Snita, D., Kubicek, M., and Marek, M. (1997) *Catal. Today*, **38**, 39.
86 Koltsakis, G.C., Konstantinidis, P.A., and Stamatelos, A.M. (1997) *Appl. Catal. B Environ.*, **12**, 161.
87 Tischer, S., Correa, C., and Deutschmann, O. (2001) *Catal. Today*, **69**, 57.
88 Tischer, S. and Deutschmann, O. (2005) *Catal. Today*, **105**, 407.
89 Maier, L., Hartmann, M., Tischer, S., and Deutschmann, O. (2011) *Combust. Flame*, **158**, 796.
90 Hartmann, M., Maier, L., and Deutschmann, O. (2010) *Appl. Catal. A Gen.* **2011**, *391*, 144.
91 Windmann, J., Braun, J., Zacke, P., Tischer, S., Deutschmann, O., and Warnatz, J. (2003) SAE Technical Paper, 2003-01-0937.
92 Braun, J., Hauber, T., Többen, H., Windmann, J., Zacke, P., Chatterjee, D., Correa, C., Deutschmann, O., Maier, L., Tischer, S., and Warnatz, J. (2002) SAE Technical Paper, 2002-01-0065.
93 Tischer, S., Jiang, Y., Hughes, K.W., Patil, M.D., and Murtagh, M. (2007) SAE Technical paper, 2007-01-1071.
94 Koop, J. and Deutschmann, O. (2009) *Appl. Catal. B Environ.*, **91**, 47.
95 Elnashaie, S.S.E.H. and Elnashaie, S.S. (1995) *Modelling, Simulation and Optimization of Industrial Fixed Bed Catalytic Reactors*, G + B Gordon and Breach.
96 Dixon, A.G. and Nijemeisland, M. (2001) *Ind. Eng. Chem. Res.*, **40**, 5246.
97 Bizzi, M., Saracco, G., Schwiedernoch, R., and Deutschmann, O. (2004) *AICHE J.*, **50**, 1289.
98 Bauer, M. and Adler, R. (2003) *Chem. Eng. Technol.*, **26**, 545.
99 Sorensen, J.P. and Stewart, W.E. (1974) *Chem. Eng. Sci.*, **29**, 827.
100 Dalman, M.T., Merkin, J.H., and McGreavy, C. (1986) *Comput. Fluids*, **14**, 267.
101 Lloyd, B. and Boehm, R. (1994) *Numer. Heat Tr. A Appl.*, **26**, 237.
102 Debus, K., Nirschl, H., Delgado, A., and Denk, V. (1998) *Chem. Ing. Tech.*, **70**, 415.

103 Logtenberg, S.A., Nijemeisland, M., and Dixon, A.G. (1999) *Chem. Eng. Sci.*, **54**, 2433.

104 Calis, H.P.A., Nijenhuis, J., Paikert, B.C., Dautzenberg, F.M., and van den Bleek, C.M. (2001) *Chem. Eng. Sci.*, **56**, 1713.

105 Petre, C.F., Larachi, F., Iliuta, I., and Grandjean, B.P.A. (2003) *Chem. Eng. Sci.*, **58**, 163.

106 Dixon, A.G., Taskin, M.E., Nijemeisland, M., and Stitt, E.H. (2008) *Chem. Eng. Sci.*, **63**, 2219.

107 Taskin, M.E., Dixon, A.G., Nijemeisland, M., Stitt, E.H. (2008) *Ind. Eng. Chem. Res.*, **47**, 5966.

108 Dixon, A.G., Taskin, M.E., Stitt, E.H., and Nijemeisland, M. (2007) *Chem. Eng. Sci.*, **62**, 4963.

109 Dixon, A.G., Nijemeisland, M., and Stitt, E.H. (2005) *Ind. Eng. Chem. Res.*, **44**, 6342.

110 Behnam, M., Dixon, A.G., Nijemeisland, M., and Stitt, E.H. (2005) *Ind. Eng. Chem. Res.*, **49**, 10641.

111 Nijemeisland, M. and Dixon, A.G. (2004) *Am. Inst. Chem. Eng. J.*, **50**, 906.

112 Yakhot, V. and Orszag, S.A. (1986) *Phys. Rev. Lett.*, **57**, 1722.

113 Laudner, B.E., and Spalding, D.B. (1974) *Comput. Methods Appl. Math. Eng.*, **3**, 169.

114 Behnam, M., Dixon, A.G., Nijemeisland, M., and Stitt, E.H. (2010) *Ind. Eng. Chem. Res.*, **49**, 10641.

115 Yuen, E.H.L., Sederman, A.J., Sani, F., Alexander, P., and Gladden, L.F. (2003) *Chem. Eng. Sci.*, **58**, 613.

116 Zakharov, V.P., Zolotarskii, I.A., and Kuzmin, V.A. (2003) *Chem. Eng. J.*, **91**, 249.

117 O'Connor, R.P., Schmidt, L.D., and Deutschmann, O. (2002) *Am. Inst. Chem. Eng. J.*, **48**, 1241.

118 Neumann, J., Golitzer, H., Heywood, A., and Ticu, I. (2002) *Rev. Chim. Bucharest*, **53**, 721.

119 de Smet, C.R.H., de Croon, M.H.J.M., Berger, R.J., Marin, G.B., and Schouten, J.C. (1999) *Appl. Catal. A Gen.*, **187**, 33.

120 Quiceno, R., Perez-Ramirez, J., Warnatz, J., and Deutschmann, O. (2006) *Appl. Catal. A Gen.*, **303**, 166.

121 (1997) FLUENT, 4.4 edn, Fluent Inc., Lebanon.

122 Raffensberger, J.A., Glasser, B.J., and Khinast, J.G. (2005) *AICHE J.*, **51**, 1482.

123 Lozano-Blanco, G., Thybaut, J.W., Surla, K., Galtier, P., and Marin, G.B. (2009) *AICHE J.*, **55**, 2159.

124 van Baten, J.M. and Krishna, R. (2004) *Ind. Eng. Chem. Res.*, **43**, 4483.

125 Troshko, A.A. and Zdravistch, F. (2009) *Chem. Eng. Sci.*, **64**, 892.

126 Kececi, S., Worner, M., Onea, A., and Soyhan, H.S. (2009) *Catal. Today*, **147**, S125.

127 Keskin, O., Worner, M., Soyhan, H.S., Bauer, T., Deutschmann, O., and Lange, R. (2010) *AICHE J.*, **56**, 1693.

128 Coltrin, M.E., Kee, R.J., Evans, G.H., Meeks, E., Rupley, F.M., and Grcar, J.F. (1991) Sandia National Laboratories.

129 Coltrin, M.E., Kee, R.J., and Evans, G. (1989) *J. Electrochem. Soc.*, **136**, 819.

130 Meeks, E., Kee, R.J., Dandy, D.S., and Coltrin, M.E. (1993) *Combust. Flame*, **92**, 144.

131 Ruf, B., Behrendt, F., Deutschmann, O., and Warnatz, J. (1996) *Surf. Sci.*, **352**, 602.

132 Kleijn, C.R. (2000) *Thin Solid Films*, **365**, 294.

133 Li, A., Norinaga, K., Zhang, W.G., and Deutschmann, O. (2008) *Compos. Sci. Technol.*, **68**, 1097.

134 Li, A.J. and Deutschmann, O. (2007) *Chem. Eng. Sci.*, **62**, 4976.

135 Kammler, H.K., Madler, L., and Pratsinis, S.E. (2001) *Chem. Eng. Technol.*, **24**, 583.

136 Kim, H., Kim, K.S., Kang, J., Park, Y.C., Chun, K.Y., Boo, J.H., Kim, Y.J., Hong, B.H., and Choi, J.B. (2011) *Nanotechnology*, **22**, 5.

137 Chub, O.V., Borisova, E.S., Klenov, O.P., Noskov, A.S., Matveev, A., and Koptyug, I.V. (2005) *Catal. Today*, **105**, 680.

138 De Greef, J., Desmet, G., and Baron, G. (2005) *Catal. Today*, **105**, 331.

139 Tsaur, K.C. and Pollard, R. (1984) *J. Electrochem. Soc.*, **131**, 975.

140 Evans, T.I., Nguyen, T.V., and White, R.E. (1989) *J. Electrochem. Soc.*, **136**, 328.

141 Gu, W.B., Wang, C.Y., and Liaw, B.Y. (1997) *J. Electrochem. Soc.*, **144**, 2053.

142 Smith, K.A., Rahn, C.D., and Wang, C.Y. (2007) *Energ. Convers. Manage.*, **48**, 2565.

143 Zhang, D., Deutschmann, O., Seidel, Y.E., and Behm, R.J. (2011) *J. Phys. Chem. C*, **115**, 468.